

Pattern formation dynamics in a Memristor Cellular Nonlinear Network structure with a numerically stable VO2 memristor model

*Original*

Pattern formation dynamics in a Memristor Cellular Nonlinear Network structure with a numerically stable VO2 memristor model / Demirkol, As; Ascoli, A; Messaris, I; Tetzlaff, R. - In: JAPANESE JOURNAL OF APPLIED PHYSICS. - ISSN 0021-4922. - ELETTRONICO. - 61:SM(2022), pp. 1-11. [[10.35848/1347-4065/ac8489](https://doi.org/10.35848/1347-4065/ac8489)]

*Availability:*

This version is available at: 11583/2988526 since: 2024-05-12T06:36:17Z

*Publisher:*

IOP Publishing Ltd

*Published*

DOI:[10.35848/1347-4065/ac8489](https://doi.org/10.35848/1347-4065/ac8489)

*Terms of use:*

This article is made available under terms and conditions as specified in the corresponding bibliographic description in the repository

*Publisher copyright*

(Article begins on next page)

PROGRESS REVIEW • OPEN ACCESS

## Pattern formation dynamics in a Memristor Cellular Nonlinear Network structure with a numerically stable $VO_2$ memristor model

To cite this article: Ahmet Samil Demirkol *et al* 2022 *Jpn. J. Appl. Phys.* **61** SM0807


View the [article online](#) for updates and enhancements.

You may also like

- [If it's pinched it's a memristor](#)  
Leon Chua
- [Towards engineering in memristors for emerging memory and neuromorphic computing: A review](#)  
Andrey S. Sokolov, Haider Abbas, Yawar Abbas et al.
- [Dynamic resistive switching devices for neuromorphic computing](#)  
Yuting Wu, Xinxin Wang and Wei D Lu



# Pattern formation dynamics in a Memristor Cellular Nonlinear Network structure with a numerically stable VO<sub>2</sub> memristor model

Ahmet Samil Demirkol<sup>\*</sup> , Alon Ascoli, Ioannis Messaris, and Ronald Tetzlaff

Chair of Fundamentals of Electrical Engineering, Technische Universität Dresden, 01069 Dresden, Germany

<sup>\*</sup>E-mail: [ahmet\\_samil.demirkol@tu-dresden.de](mailto:ahmet_samil.demirkol@tu-dresden.de)

Received February 21, 2022; revised July 13, 2022; accepted July 27, 2022; published online August 19, 2022

In this work, we explore pattern formation dynamics across a diffusively coupled Memristor Cellular Nonlinear Network (MCNN), which is composed of identical cells with locally active memristors. We bias the cells on the edge-of-chaos, introduce a systematic design procedure to induce complexity in the array, and extract the element values analytically in a parametric form. In order to enhance the stability and speed of the numerical simulations, we apply a simple variable transformation to a core memristor model while we include the additional effect of parasitic resistors to investigate the locally active dynamics of a VO<sub>2</sub> device. We first take a close look at the effect of the linear coupling resistor on pattern formation, and later study how nonlinearly-resistive coupling, based upon tangent hyperbolic law, affect the emergence of complex patterns. Simulation results reveal that a variety of static patterns with different characteristics can emerge across the proposed MCNN.

© 2022 The Author(s). Published on behalf of The Japan Society of Applied Physics by IOP Publishing Ltd

## 1. Introduction

The dimensions of microelectronic circuits have been aggressively scaled down since the first implementation of integrated circuits (ICs) in 1960s. This downscaling has not only boosted the technological developments but also resulted in a huge market size for consumer electronics with a significant demand on artificial intelligence (AI) technologies. Since reaching atomic boundaries in semiconductor technology has announced the practical end of the Moore's law already a decade ago, the electronic industry is compelled to develop novel materials and computing strategies to overcome the Von-Neumann bottleneck of conventional computing systems.<sup>1,2</sup> In line with these expectations, the intentional realization of memristors,<sup>3</sup> a novel nanoscale resistive memory element theoretically postulated<sup>4</sup> in the early seventies, led to the development of a new paradigm called in-memory computing.<sup>5,6</sup> Since 2008, when Hewlett Packard Labs announced the observation of memristive phenomena in resistance switching devices based on thin oxide films, there has been a huge research on fabrication, modeling, and implementation of memristor-based systems.

Due to the fact that memristors can perform computing and data storage tasks inherently inside the same media, the need for joining the computing and memory units can be eliminated in memristive computing architectures. The performance improvement, which this provides to electronics, immediately suggests the design of novel circuits and systems which are suitable for typical AI computations within the Internet-of-Things (IoT) and Data-Processing-on-the-Edge concept. For instance, memristors employed in crossbar architectures,<sup>7,8</sup> can be quite useful for the design of hardware accelerators for running deep learning algorithms in AI systems. Likewise, exploiting their extremely small size fingerprints, memristors can be utilized in the design of dense logic and memory blocks.<sup>9,10</sup> Furthermore, locally active volatile memristors can be engaged in the emulation of neural circuits<sup>11,12</sup> generating action potentials while multi-state non-volatile memristors are particularly suitable for the

realization of synaptic circuits,<sup>13</sup> indicating a promising future for the design of bio-inspired systems.

Biological neural networks can implement cognitive tasks such as associative memory or real time sensory data processing in an area and power efficient way. Therefore, the effectiveness and functionality of the neural systems have been studied thoroughly while there is a continuing research interest in the field of computational neuroscience,<sup>14,15</sup> roots dating back to the early 1900s.<sup>16</sup> Consequently, the design of neuromorphic circuits, which mimic the behavior of biological neural networks in an area of power efficient way, has been popular for several decades.<sup>17,18</sup> Inspired from its biological counterpart, Cellular Neural/Nonlinear Networks (CNNs), which can be defined as homogeneous structures composed of regularly spaced and locally coupled identical cells, was suggested<sup>19</sup> as an efficient hardware solution to implement cognitive tasks such as image processing in continuous period of time. It has been shown that many complex problems, such as pattern formation, locomotion control, modelling reaction-diffusion systems, based upon partial differential equations, can be solved by properly mapping them on CNNs.<sup>20,21</sup> Furthermore, it has been shown that, resistively coupled CNNs may implement spatially-discretized versions of reaction-diffusion equations and, having their isolated cells biased on the edge-of-chaos (EOC), they constitute ad hoc hardware structures for the reproduction of pattern formation.<sup>22,23</sup>

Pattern formation, also known as emergent phenomenon, occurs in various scientific disciplines.<sup>24</sup> Following the seminal paper of Turing,<sup>25</sup> its mathematical basis has been thoroughly studied via reaction-diffusion partial differential equations.<sup>26</sup> Specifically, pattern formation is believed to establish the basis of neural oscillations, which take place during different cognitive processes. Several pattern formation examples<sup>27,28</sup> have been recently presented through resistively coupled Memristor Cellular Nonlinear Networks (MCNNs) employing locally active memristor models. Recently, we have presented the analytical investigation of pattern formation dynamics in MCNNs where we derived



necessary conditions for the appearance of emergent phenomena in a parametric form.<sup>29–31</sup>) Precisely, this was implemented by taking into account the requirements established by the theory of local activity and examining the effect of design parameters on the complex behaviors of the bio-inspired arrays.<sup>29–31</sup>)

In this work, we investigate pattern formation dynamics in an MCNN, where we employ an experimentally verified model which is able to reproduce the rich dynamics of a VO<sub>2</sub> memristor device.<sup>32</sup>) In particular, the equations that describe experimental characteristics of the VO<sub>2</sub> device are based upon a threshold switch model, first developed by Pickett<sup>33</sup>) to reproduce the nonlinear dynamics of a similar cell based upon NbO. As a novelty of this work, in order to enhance the stability and speed of the numerical simulations, we introduce a variable transformation in the Pickett model. After that, by including parallel and series resistors in the mathematical description, we perform a systematic investigation of the small signal and locally active dynamics of the overall VO<sub>2</sub> device which is known to exhibit extremely rich dynamical characteristics. Then, we introduce the stability analysis of a compact VO<sub>2</sub> memristor-based MCNN cell and extract its circuit parameter set in the EOC region. Similarly, we present the instability analysis of the same cell, taking into account the respective coupling circuitry within the proposed array and extract qualitatively the coupling parameter set in the sharp-EOC region. Differently from previous works, we show that changing the capacitance value for the capacitor inside the cell can affect static pattern formation in the array. Most importantly, we take a close look at the effect of the linear coupling resistor on the pattern characteristics exploring the location of static equilibria on the DC current–voltage curve of the memristor so as to show that the operating points lying in the locally active and passive regions can simultaneously store different patterns. We carry out a similar analysis after replacing the linear coupling resistor with a nonlinear tangent hyperbolic resistor and show that such a replacement introduces a clear contrast in the patterns, improving their detection in view of a future application. Importantly, an extensive number of numerical simulation results reveal that a variety of static patterns with different characteristics can emerge across the proposed MCNN depending on the design parameter choice.

## 2. Experimental methods

In this work, we bring to the readers’ attention a threshold switching device model that is based on the Joule heating rate of a thermally driven insulator-to-metal phase transition in a volatile memristor. This model was first proposed by Pickett and Williams<sup>33</sup>) (thus referred as Pickett model in the following text) and initially introduced to accurately reproduce the experimental data of current-controlled (CC) negative differential resistance (NDR) NbO devices. Additionally, the Pickett model can be employed to represent a broader class of threshold switching devices. For instance, as demonstrated in Ref. 32 and in the respective supplementary information file in detail, the Pickett model can also successfully replicate the experimental characteristics of a VO<sub>2</sub> device. Briefly, this was achieved after the inclusion of parallel and series resistors into the mathematical description and running the parameter fitting procedure once again. In this way, a very good matching between experimental

and simulation data, pertaining to various neural behaviors, was reported. In the design of the proposed MCNN cells, we employ a comprehensive locally active VO<sub>2</sub> memristor model, introducing its detailed circuit theoretic analysis in the following subsection. Later, we shall present the stability analysis for the single cell of the proposed MCNN, as well as the instability analysis for the coupled cell configuration.

### 2.1. Variable transformation in Pickett’s threshold switching memristor model

The equations describing the Pickett model are given in Eqs. (1)–(5) where  $u \triangleq r_{\text{met}}/r_{\text{ch}}$  stands for the state variable and  $u \in (0, 1)$ . Further discussion about the Pickett model can be found in Ref. 33.

$$v = R(u) \cdot i \tag{1}$$

$$\frac{du}{dt} = (H(u))^{-1} \cdot (i^2 \cdot R(u) - \Gamma(u) \cdot \Delta T) \tag{2}$$

$$R(u) = \frac{\rho_{\text{ins}} L_{\text{ch}}}{\pi r_{\text{ch}}^2} \cdot \left[ 1 + \left( \frac{\rho_{\text{ins}}}{\rho_{\text{met}}} - 1 \right) \cdot u^2 \right]^{-1} \tag{3}$$

$$\Gamma(u) = 2\pi L_{\text{ch}} \kappa \cdot \left( \ln \frac{1}{u} \right)^{-1} \tag{4}$$

$$H(u) = \pi L_{\text{ch}} r_{\text{ch}}^2 \cdot \left( \Delta T c_p \cdot \frac{1 - u^2 + 2u^2 \ln u}{2u(\ln u)^2} + 2\Delta h_{\text{tr}} \cdot u \right). \tag{5}$$

During the current and voltage sweep simulations in the Matlab environment, it was noticed that the Pickett model can exhibit numerical instability issues depending on the choice of the input signal characteristics. It was observed that the state variable can attain values outside the range (0,1) during the simulations and undergo multiple inconsistent sharp jumps depending on the simulation settings, even if the state is forced to be confined within the range (0,1) through a limiter function. Likewise, the model requires a long simulation time during the investigation of the device DC  $I$ – $V$  characteristics. In order to cope with these numerical complications and relax the tolerance settings for the numerical solver, we apply a variable transformation in the Pickett model. In particular, we define a new state variable  $x$  such that  $u = \exp\left(-\frac{x_a}{x - x_s}\right)$ . Here,  $x_a$  and  $x_s$  are constants, which are introduced in order to apply amplitude scaling and shifting to the state variable, respectively, and the new state variable  $x$  gets values in the interval  $(x_s, \infty)$ . After applying the variable transformation, it is possible to cast the original model formulas from Eqs. (1)–(5) as given in Eqs. (6)–(9) where  $g_c, g_0, g_1, k$  and  $C_c$  are simple combinations of the Pickett model parameters, introduced here for a compact representation

$$i = G(x) \cdot v \tag{6}$$

$$C(x) \cdot \frac{dx}{dt} = v^2 \cdot G(x) - g_c \cdot (x - x_s) \tag{7}$$

$$G(x) = g_0 + g_1 \cdot \exp\left(-\frac{2x_a}{x - x_s}\right) \quad (8)$$

$$C(x) = C_c \left[ 1 - \exp\left(-\frac{2x_a}{x - x_s}\right) \left( 1 + \frac{2x_a}{x - x_s} - k \left( \frac{2x_a}{x - x_s} \right)^2 \right) \right] \quad (9)$$

We would like to note that the state dependent function  $C(x)$  has a contribution during the voltage and current sweeps for relatively high frequencies only (e.g.  $f \geq 10$  MHz), while it can be assumed as a constant for quasi-static characterization. Most importantly, the application of the variable transformation reveals that the differential algebraic equation (DAE) set of the original Pickett model belongs to the same class as models of other NDR devices,<sup>34,35</sup> where a Poole-Frenkel conduction mechanism lies at the origin of volatile resistance switching phenomena. Moreover, each of the DAE sets of the original and transformed Pickett models, i.e. Eqs. (1)–(5), and Eqs. (6)–(9), respectively, falls in the family of generic memristors, as is the case for most NDR device models proposed earlier in the literature. We depict in Fig. 1 the DC  $I$ - $V$  plot of the Pickett model, demonstrating a current-controlled characteristic, where two positive differential resistance (PDR) regions separate an NDR branch.

### 2.2. Numerically stable locally active VO<sub>2</sub> memristor model

Although Eqs. (1)–(5) and Eqs. (6)–(9) are identical and represent the same system, it was confirmed through several numerical simulations that the latter set of equations is numerically stable (e.g. the inconsistent sharp jumps in the state variable in the original model are eliminated), and requires shorter simulation time for the same tolerance settings as in the original set of equations. Furthermore, in order to match experimental data extracted from a VO<sub>2</sub> device, Ref. 32 recommends to connect parallel and series resistors to the core device represented by Eqs. (6)–(9). The current-voltage relationship and the state equation of the complete device, including the contributions of series and parallel resistors,  $R_s$  and  $R_p$ , respectively, are in turn given in Eqs. (10) and (11), where  $G_p = R_p^{-1}$ .

$$i_m = [R_s + (G(x) + G_p)^{-1}]^{-1} \cdot v_m \quad (10)$$

$$C(x) \cdot \frac{dx}{dt} = [1 + R_s(G(x) + G_p)]^{-2} \cdot v_m^2 \cdot G(x) - g_c \cdot (x - x_s). \quad (11)$$

The DC current-voltage ( $I_m$ - $V_m$ ) characteristics of the complete memristor, together with its schematic, are given in Fig. 2, where the effects of  $R_s$  and  $R_p$  on the DC  $I_m$ - $V_m$  characteristic are further highlighted. Here, the slope of the lower PDR region (PDR1) is dominated by  $R_p$  while the slope of the upper PDR region (PDR2) is dominated by  $R_s$ . To gain a deeper insight, we divide the branch between PDR1 and PDR2 regions of the DC  $I_m$ - $V_m$  curve of the complete device into 3 regions (these regions will be shown to be locally active in the following sub-section) and label them as LA1, LA2, and LA3, where the union of LA1 and LA2 represents the NDR region of the overall device. Comparing Figs. 1 and 2, it can be observed that DC characteristic of the complete device, as a distinctive property, has a positive slope in region LA3. This property indeed shows itself as a horizontal jump through voltage values during a current sweep, as depicted by the green lines in Fig. 2. Here, it should be noted that the equilibria in region LA3 are never visited during such a current sweep while the equilibria in region LA2, where the differential resistance is negative, are visited only during the decremental phase of the input. On the other hand, being a single valued function of the device current, region LA1 region keeps featuring similar qualitative characteristics as the corresponding one on the NDR branch of the core device and can be visited in both phases of a current sweep.

### 2.3. AC equivalent model of the VO<sub>2</sub> memristor

Small-signal models may provide peculiar information about the local dynamics of nonlinear systems. In this regard, it is essential to utilize the AC equivalent model of the VO<sub>2</sub> device to gain further insights. Derivation of AC equivalent models of locally active memristor with different mathematical models have been recently presented in the literature where, different circuit topologies were proposed<sup>36,37</sup> for the basic cell of bio-inspired cellular arrays. Derived in Ref. 38 and utilized in Refs. 29 and 31 here we adopt Foster's first

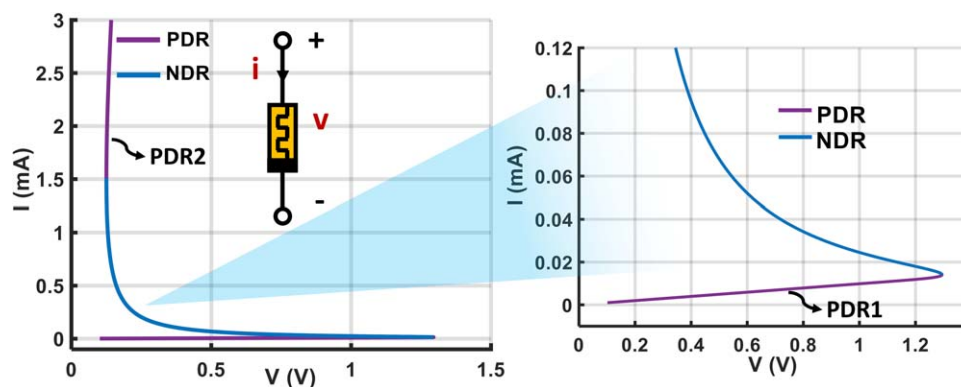


**Fig. 1.** (Color online) DC  $I$ - $V$  characteristic of the core VO<sub>2</sub> memristor according to the Pickett model. The current-controlled NDR region, drawn in blue color, is further zoomed in to improve the quality of its graphical illustration. The upper and lower purple traces represent the PDR2 and PDR1 branches. Their union composes the locally-passive NDR region.

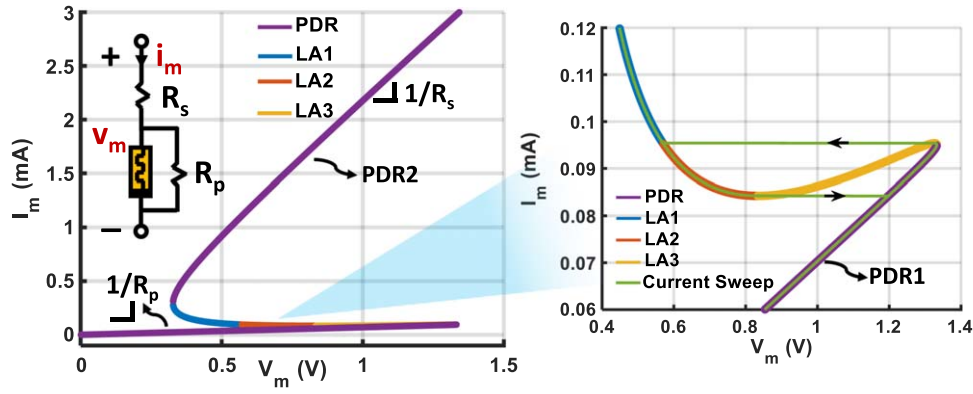


**Fig. 2.** (Color online) DC  $I_m$ - $V_m$  characteristics of the overall  $\text{VO}_2$  device in the inset. Note that  $V_m$  is not a single valued function of  $I_m$ , while  $R_s$  and  $R_p$  dominate the slope of the upper and lower PDR region, respectively. The locally active portion of the DC  $I_m$ - $V_m$  characteristic, which lies between the two PDR regions, is divided into 3 branches, called LA1, LA2, and LA3. These regions are further zoomed in, resulting in a clearer illustration.  $V_m$  is a single valued function of  $I_m$  along the LA1 branch. On the other hand, over the common current range for the LA2 and LA3 branches,  $V_m$  is a triple-valued function of  $I_m$ , which explains the horizontal jumps observed under current sweep (see the green lines).

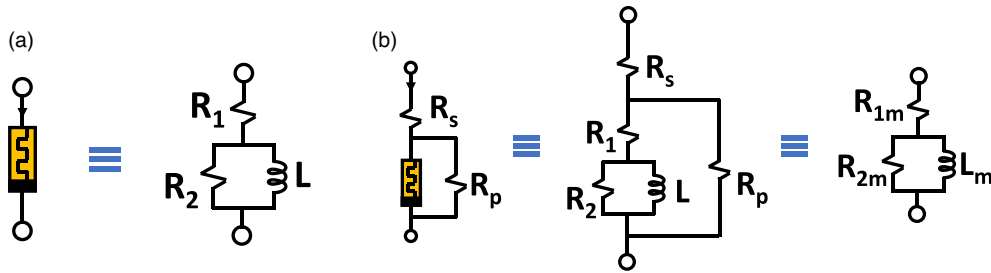


**Fig. 3.** (Color online) (a) AC equivalent circuit of the core memristor. (b) Visualization of the procedure to obtain the AC equivalent circuit of the complete device. Both memristors feature the same type of AC equivalent where  $R_{1m}$  ( $R_1$ ) corresponds to the slope of the DC  $I$ - $V$  curve, the sum  $(R_{1m} + R_{2m})$  ( $(R_1 + R_2)$ ) defines the instantaneous resistance  $V_m/I_m$  ( $V/I$ ) and  $L_m$  ( $L$ ) represents the device dynamics.

form for the RL circuit configuration<sup>39)</sup> of the local model of the core memristor, which is illustrated in Fig. 3(a). In the AC equivalent circuit of the core memristor,  $R_1$  represents the inverse of the slope of the DC  $I$ - $V$  curve and naturally assumes negative values in the NDR region. The quantity  $(R_1 + R_2)$  corresponds to the instantaneous resistance (i.e.  $V/I$ ) of the core memristor, which inherently gets always positive values since the  $I$ - $V$  curve may only reside in the first and third quadrants.  $L$  represents the dynamics of the core device. Finally,  $L$  and  $R_2$  have positive values at all equilibrium points.

The procedure to obtain the AC equivalent circuit of the complete device is illustrated in Fig. 3(b) where we replace the core memristor with its linear equivalent model and derive the AC circuit of the complete device. After a simple rearrangement of the circuit elements, it is possible to cast the final version of the AC equivalent circuit in a RL circuit form, once again.

Here, we note that since the core memristor and the complete device possess the same form of AC equivalent circuit topology, we may conclude that  $R_{1m}$  corresponds to the inverse of the slope of the DC  $I_m$ - $V_m$  curve while the sum  $(R_{1m} + R_{2m})$  defines the instantaneous resistance  $V_m/I_m$ , which always attains positive values. The exact expressions for the AC circuit elements of the complete device in terms of the core device element values as well as of  $R_s$  and  $R_p$  are given in Eqs. (12)–(14)

$$R_{1m} = R_1 \cdot \frac{R_p}{R_1 + R_p} + R_s \tag{12}$$

$$R_{2m} = R_2 \cdot \frac{R_p}{R_1 + R_p} \cdot \frac{R_p}{R_1 + R_2 + R_p} \tag{13}$$

$$L_m = L \left( \frac{R_p}{R_1 + R_p} \right)^2 \tag{14}$$

Referring to the right plot of Fig. 2 and focusing on the LA region, it can be deduced from Eq. (12) that, when the polarity of the term  $(R_1 + R_p)$  goes negative, which is the case in the branch LA3,  $R_{1m}$  attains positive values. Likewise, it can be concluded from Eq. (13) that, when  $(R_1 + R_p)$  attains a negative sign, i.e. along the LA3 branch,  $R_{2m}$  becomes negative as well. Recall that, on the other hand, the corresponding parameter in the core device local circuit model, namely  $R_2$ , is strictly positive. Thus, the common dependency of  $R_{1m}$  and  $R_{2m}$  on the term  $(R_1 + R_p)$  implies that  $R_{1m}$  and  $R_{2m}$  change their signs simultaneously. Finally, it can be seen from Eq. (14) that  $L_m$  always gets positive values, as the element  $L$  of the core device in the local circuit model does. Table I summarizes the polarities of the parameters in the small signal equivalent circuit model of the overall device, shown in the inset within the left plot of Fig. 2, as well as some of the other critical terms, for each of

**Table I.** Polarities of the AC circuit elements and of some other critical terms in each of the three branches LA1, LA2, and LA3 of the DC  $I_m$ - $V_m$  locus of the complete device.

	$R_1 + R_p$	$R_{1m}$	$R_{2m}$	$L_m$	$R_{1m} + R_{2m}$
LA1	>0	<0	>0	>0	>0
LA2	>0	<0	>0	>0	>0
LA3	<0	>0	<0	>0	>0

the three locally active regions in the DC  $I_m$ - $V_m$  characteristic of the device itself. Lastly, we plot  $R_1$  and  $R_{1m}$  together in Fig. 4(a), versus all the possible equilibria in the locally active region LA of the corresponding device. We then plot  $R_2$  and  $R_{2m}$  together in Fig. 4(b) versus the same set of equilibrium points. It can be appreciated from Fig. 4 that,  $R_{1m}$  and  $R_{2m}$  have qualitatively similar characteristics but hold opposite signs.

**2.4. Stability and local activity analysis of the VO<sub>2</sub> device**

In order to examine the stability of the complete device, we refer to the AC equivalent circuit of Fig. 3(b) and introduce its local impedance function  $Z(s)$  (equivalently the admittance function  $Y(s) = 1/Z(s)$ ) in Eq. (15)

$$Z(s) = \frac{sL(R_{1m} + R_{2m}) + R_{1m}R_{2m}}{sL + R_{2m}} \tag{15}$$

The poles of the impedance function define the stability of a given equilibrium point when the input is a current signal. Similarly, the zeros of  $Z(s)$  (corresponding to the poles of the admittance function  $Y(s)$ ) define the stability of a given equilibrium point when the input is a voltage signal. Since  $Z(s)$  has a right hand side (RHS) pole for  $R_{2m} < 0$ , we can conclude from Table I that the memristor device is unstable during a current sweep for each equilibrium point lying in LA3, which explains the horizontal jumps that are depicted on the right plot of Fig. 2. Furthermore,  $Z(s)$  owns a RHS zero over the entire locally active region ( $LA = LA1 \cup LA2 \cup LA3$ ) since  $z = -R_{1m}R_{2m}/L(R_{1m} + R_{2m}) > 0$  according to Table I, implying instability of each equilibrium along the entire LA region for the voltage driven case.

In order to promote pattern formation in a diffusively coupled network, it is essential for the latter to own locally active elements which can exhibit unstable dynamics under certain conditions. In this regard, local activity can be considered as the

violation of local passivity where all the dynamics are strictly stable. Furthermore, a locally active element is defined to be on the EOC as long as it is asymptotically stable. A rigorous definition with criteria for local activity can be found in Ref. 23 while the application of these criteria through the local activity analysis of a memristive cell can be found in Refs. 29,30. Here, we adopt a practical approach and confirm that the memristor under investigation is locally active in LA1, LA2, and LA3 regions due to the existence of the RHS zero, as mentioned above, which cannot be accommodated by a locally-passive element. Then, under current input, the VO<sub>2</sub> device is said to be on the EOC in LA1 and LA2 regions where  $Z(s)$  has a left hand side (LHS) pole (i.e.  $p = -R_{2m}/L < 0$ ) and is therefore asymptotically stable. Finally, the current-controlled VO<sub>2</sub> memristor is locally active but unstable in LA3, since the pole of  $Z(s)$  resides on the right half plane.

**2.5. The basic MCNN cell: stability, local activity, and destabilization after coupling**

The basic 2nd order cell employed in this work is presented in Fig. 5(a) where  $I_b$  is a DC current source,  $R_b$  is a bias resistor,  $C$  is a capacitor in parallel with the memristor and the coupling node is denoted by an open circle.

For the emergence of complex behavior through a homogenous medium, the isolated cell has to be poised on the EOC, implying local activity with stability or a “silent” state with hidden excitability for the cell. In order to investigate stability and local activity conditions for the cell in Fig. 5(a), we apply the strategy introduced in Ref. 40 and utilize the AC equivalent circuit, which is illustrated in Fig. 5(b). The impedance function  $Z_{sc}(s)$  of the cell small signal equivalent circuit, as appearing between the coupling node and ground, is given in Eq. (16)

$$Z_{sc}(s) = \frac{R_b[sL_m(R_{1m} + R_{2m}) + R_{1m}R_{2m}]}{s^2L_mC(R_{1m} + R_{2m})R_b + s[L_m(R_{1m} + R_{2m} + R_b) + R_{1m}R_{2m}R_bC] + (R_{1m} + R_b)R_{2m}} \tag{16}$$

To ensure the stability for the cell,  $Z_{sc}(s)$  has to feature LHS poles only, which enforces the inequalities  $(R_{1m} + R_b)R_{2m} > 0$  and  $L_m(R_{1m} + R_{2m} + R_b) + R_{1m}R_{2m}R_bC > 0$  to be satisfied. According to Table I, the first inequality is satisfied if and only if  $R_{2m} > 0$  and  $R_{1m} + R_b > 0$ , suggesting that the device has to be biased either in branch LA1 or in branch LA2. The stability conditions under this assumption can be derived as given in Eqs. (17) and (18)

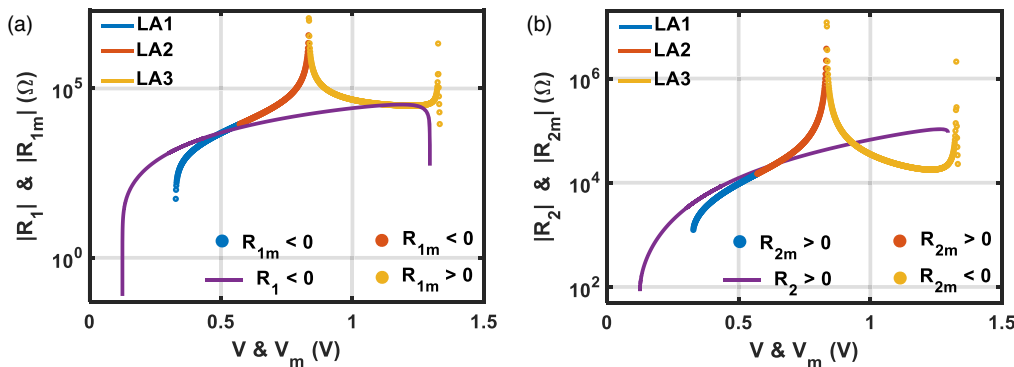


**Fig. 4.** (Color online) (a)  $R_1$  and  $R_{1m}$  and (b)  $R_2$  and  $R_{2m}$  versus all the possible equilibria in the LA regions of corresponding device.  $R_1$  is always negative since the NDR and locally active regions of the core memristor overlap, while  $R_{1m}$  attains positive value in region LA3. Likewise,  $R_2$  is always positive while  $R_{2m}$  reads negative values in region LA3. It should be noted that  $R_{1m}$  and  $R_{2m}$  always have opposite signs while their sum ( $R_{1m} + R_{2m}$ ) can attain positive values only.

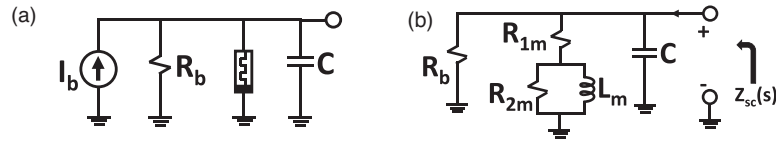


**Fig. 5.** (Color online) (a) Basic cell of the MCNN structure where  $I_b$  is the DC current source,  $R_b$  is the bias resistor,  $C$  is the parallel capacitor and open circle denotes the coupling node. (b) AC equivalent of the cell in (a) where  $Z_{sc}(s)$  is the impedance function appearing between the coupling node and ground.

$$R_{1m} + R_b > 0 \quad (17)$$

$$C < -\frac{L_m(R_{1m} + R_{2m} + R_b)}{R_{1m}R_{2m}R_b} = C_{\max}. \quad (18)$$

Once the device is biased either in branch LA1 or in branch LA2, inspecting Eq. (16) and Table I, it can be realized that  $Z_{sc}(s)$  features a RHS zero (i.e.  $z = -R_{1m}R_{2m}/L(R_{1m} + R_{2m}) > 0$ ), and, as a result, cannot be implemented via a locally passive one-port. Therefore, we conclude that the isolated cell is both locally active and stable, i.e. on the EOC, as long as the device is biased either in branch LA1 or in branch LA2 and the conditions given by Eqs. (17) and (18) are satisfied.

With the single cell poised on the EOC, resistive coupling between the identical cells can destabilize the “silent” cells and promote pattern formation<sup>41</sup> in the resulting network. A simple yet highly accurate method<sup>23</sup>) to investigate the destabilization “potential” of coupled cells is to terminate the coupling node of a single cell (see the exemplary unit of Fig. 5(a), for example) with a coupling resistor  $R_c$  and investigate the stability of the resulting simple network through the analysis of its AC equivalent circuit model. In this case,  $R_c$  will appear in parallel with  $R_b$  from the AC equivalent circuit model of Fig. 5(b). Therefore, the condition for destabilizing the basic cell of our MCNN, by adding a single resistor  $R_c$  between its coupling node and ground [refer to Fig. 5(a)], can be obtained by a simple replacement of  $R_c$  with the parallel equivalent  $R_b \parallel R_c$  in Eq. (16). This replacement updates the formula for the local impedance  $Z_{sc}(s)$ , indicated in Fig. 5(b), according to the new cell topology. More details on this procedure can be found in Ref. 40. Applying the theorem of local activity for the new formula of  $Z_{sc}(s)$ , the destabilization condition for the cell of Fig. 5(a) under the simple resistive coupling scenario is given by Eq. (19). This inequality defines a constraint on the dissipative environment, which, together with the conditions (17)–(18), forms the so-called sharp-EOC parameter set and promotes the emergence of complexity in the overall network

$$R_c < -\frac{R_{1m} \cdot R_b}{R_{1m} + R_b} = R_{c-\max} = -(R_{1m} \parallel R_b). \quad (19)$$

We depict  $C_{\max}$  and  $R_{c-\max}$  as a function of the equilibrium points in the branches LA1 and LA2 in Fig. 6. Here,  $C_{\max}$  and  $R_{c-\max}$  are clearly inversely proportional one to the other.

Finally, we present three different DC biasing scenarios for the VO<sub>2</sub> device inside the cell. In this regard, for each cell of the network, we fix the bias resistance  $R_b$  to 50 kΩ and tune the bias current through each value in the set  $I_b = \{100, 110, 150\} \mu\text{A}$ . The intersections between the DC  $I_m$ - $V_m$  locus of the VO<sub>2</sub> device and the load lines, each associated to one of the aforementioned three DC bias current values, are graphically illustrated in Fig. 7. Here, filled circles

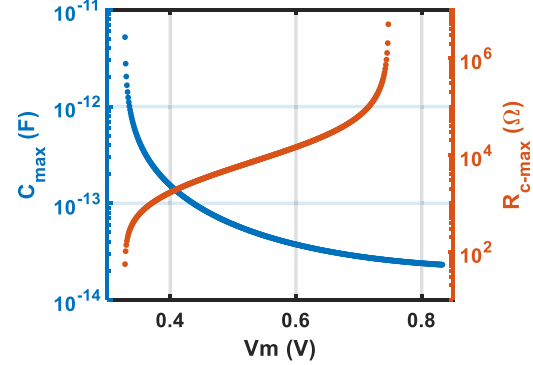


**Fig. 6.** (Color online)  $C_{\max}$  and  $R_{c-\max}$  versus all equilibria in across the union of regions LA1 and LA2, where the cell can be biased on the edge-of-chaos. Note that  $C_{\max}$  and  $R_{c-\max}$  have inversely proportional characteristics in these regions.

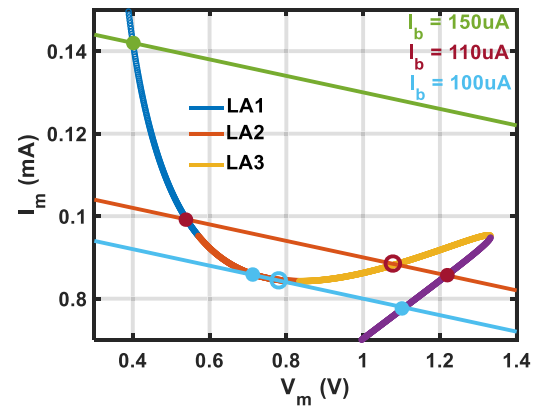


**Fig. 7.** (Color online) Intersection between three different load lines with the DC  $I_m$ - $V_m$  curve, defined for  $R_b = 50 \text{ k}\Omega$  and each  $I_b$  value from the set  $\{100, 110, 150\} \mu\text{A}$ . Here, filled (open) circles denote stable (unstable) DC operating points for the VO<sub>2</sub> device inside the basic cell.

indicate the locations of the stable DC operating points of the single cell. On the other hand, open circles indicate the locations of the unstable DC operating points as well. We note that, for  $I_b = 100 \mu\text{A}$ , the condition given by Eq. (17) is satisfied only for the operating point denoted with the filled circle lying in LA2 region.

### 3. Results and discussion

The proposed MCNN has a 2D grid form where all the  $35 \times 35$  constitutive cells are identical one to the other and resistively coupled to the respective nearest neighbors only. Moreover, periodic boundary conditions are imposed to define the dynamics of the network at its borders. The pattern configurations to be presented in this work are obtained for three different DC bias current values, precisely those in the set  $I_b = \{100, 110, 150\} \mu\text{A}$ . Furthermore, we set the same initial conditions for all the cells, except the cell in the center of the network. Specifically, we choose a stable DC operating



point of the basic cell, which emerges either in the LA1 branch or in the LA2 branch depending upon the  $I_b$  choice (refer to Fig. 7), as the initial condition for each unit in the proposed MCNN. For  $I_b = 150 \mu\text{A}$ , initial condition for the center cell is fixed to a slightly-perturbed version of the common initial condition chosen for the other cells. For each  $I_b$  value in the set  $I_b = \{100, 110\} \mu\text{A}$ , the stable DC operating point of the basic cell, which lies in the PDR1 region (refer to Fig. 7), is assigned to the initial condition of the center cell.

### 3.1. Static pattern formation

In this sub-section we investigate static pattern formation dynamics in the proposed MCNN, and present new findings which we never reported earlier. We firstly examine the effect of the parallel capacitor on pattern formation. We set  $I_b = 150 \mu\text{A}$ ,  $R_b = 50 \text{ k}\Omega$ ,  $R_c = 4 \text{ k}\Omega$  and vary the capacitance value through each value in the set  $C = \{10, 50, 100\} \text{ fF}$ . Results are shown in Fig. 8, where we visualize the steady-state value of the memristor voltage in each cell of the network, according to the given color coding map, for the first, second, and third capacitance value in the aforementioned set.

In the next step, we explore the effect of the coupling strength on the pattern characteristics as well as on the distribution of the equilibrium points of all the cells of the network along the DC  $I_m$ - $V_m$  curve of the  $\text{VO}_2$  device. We set  $I_b = 100 \mu\text{A}$ ,  $R_b = 50 \text{ k}\Omega$ ,  $C = 10 \text{ fF}$  and vary the coupling resistance through each value in the set  $R_c = \{0.5, 2.5, 10\} \text{ k}\Omega$ . Results are depicted in Fig. 9 where, plots (a)–(c) visualize the memristor voltages across the MCNN according to the aforementioned color coding map, and plots (d)–(f) define ternary patterns, illustrating whether the equilibrium of each cell of the array is located along the PDR1 branch, or the LA branch, or the PDR2 branch, using a shade of gray, red, or yellow, to color the pixel in the relevant position across the  $35 \times 35$  grid, respectively.

We continue our investigation on the impact of the local resistive connections between the cells on pattern formation dynamics by replacing the linear coupling resistor with a nonlinear one with tanh characteristics, as shown in Fig. 10. We vary  $I_b$  through each value in the set  $I_b = \{100, 110, 150\} \mu\text{A}$ , while we set  $R_b = 50 \text{ k}\Omega$ , and  $C = 10 \text{ fF}$ . As for the local resistive connections between the cells, we either choose a linear resistor of resistance  $R_c = 1 \text{ k}\Omega$ , or a nonlinear resistor obeying the constitutive relationship  $I_{Rc} = 5 \cdot 10^{-5} \cdot \tanh(20 \cdot V_{Rc})$ . Figures 11(a)–11(c), 11(g)–11(i) and 11(m)–11(o) visualize the simulation

results obtained in the linear coupling case. Figures 11(d)–11(f), 11(j)–11(l) and 11(p)–11(r) illustrate the simulation results obtained in the nonlinear coupling case. Here, each of the Figs. 11(a)–11(f) provides a graphical representation for the memristors' steady-state voltage values throughout the MCNN for the respective simulation scenario, according to the color coding map defined in the legend. Each of the Figs. 11(g)–11(l) illustrates whether, in the respective simulation, the equilibrium of each MCNN cell is found to lie in the PDR1 branch, or in the LA branch, or, rather, in the PDR2 branch of the DC  $I_m$ - $V_m$  characteristic, employing a gray, or a red, or, rather, a yellow color for the pixel in the relevant position across the  $35 \times 35$  grid, respectively. Finally, each of the Figs. 11(m)–11(r) shows the spatial distribution of the MCNN cells' DC operating points along the same  $I_m$ - $V_m$  locus, for the corresponding simulation.

Finally, we examine the transient characteristics of the cell capacitor (or equivalently memristor) voltages for different emerging patterns. For this purpose, we set  $I_b = 110 \mu\text{A}$ ,  $R_b = 50 \text{ k}\Omega$ ,  $C = 10 \text{ fF}$  and vary the coupling resistance through each value in the set  $R_c = \{0.2, 2, 20\} \text{ k}\Omega$ . The results are shown in Fig. 12 where the first, second and third rows represent the cases  $R_c = 0.2 \text{ k}\Omega$ ,  $R_c = 2 \text{ k}\Omega$ , and  $R_c = 20 \text{ k}\Omega$ , respectively. Here, plots (a), (c), (e) illustrate the memristor voltages across the MCNN according to the given color coding map, while plots (b), (d), (f) introduce the transient characteristics of cell capacitor voltages until they settle down to the respective steady-state values.

### 3.2. Discussion

Inspecting Fig. 8, it may be realized that, although it does not play a role on the DC solution of the network, the cell capacitance has an impact on the static patterns emerging in the array. This fact implies that the transient solution of the network can be modulated via the capacitance value and, as a result, evolve toward one among a number of different heterogeneous patterns. This observation further points that, another approach to affect the transients of the network so as to influence the emerging patterns envisages the tuning of the cells' initial conditions.

Comparing the three plots in Figs. 9(a)–9(c), it may be concluded that the color transition between a cell and its direct neighbors is rather smooth in the strong coupling scenario [see Fig. 9(a)], while it becomes sharper as the coupling strength is reduced [see Fig. 9(c)]. As a novel investigation, looking now at the three plots in Figs. 9(d)–9(f), it may be realized that, in the strong coupling scenario [see Fig. 9(d)], most of the DC equilibria of the MCNN cells

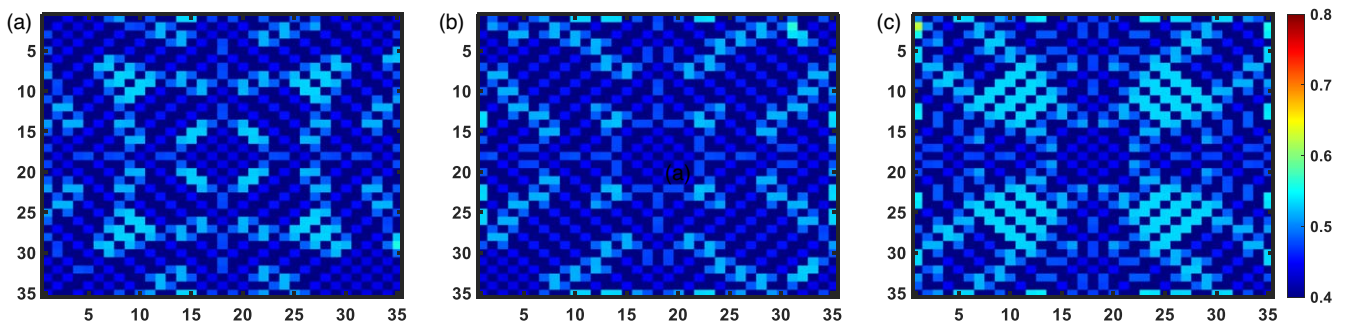


**Fig. 8.** (Color online) Simulation results of a  $35 \times 35$  MCNN structure for  $I_b = 150 \mu\text{A}$ ,  $R_b = 50 \text{ k}\Omega$ ,  $R_c = 4 \text{ k}\Omega$ , while  $C = 10 \text{ fF}$  in (a),  $C = 50 \text{ fF}$  in (b), and  $C = 100 \text{ fF}$  in (c). All the cells have the same initial condition except for the one in the center of the network. It can be seen that the capacitance dependent transient solutions of the network may affect the type of static pattern, which arises at steady state.

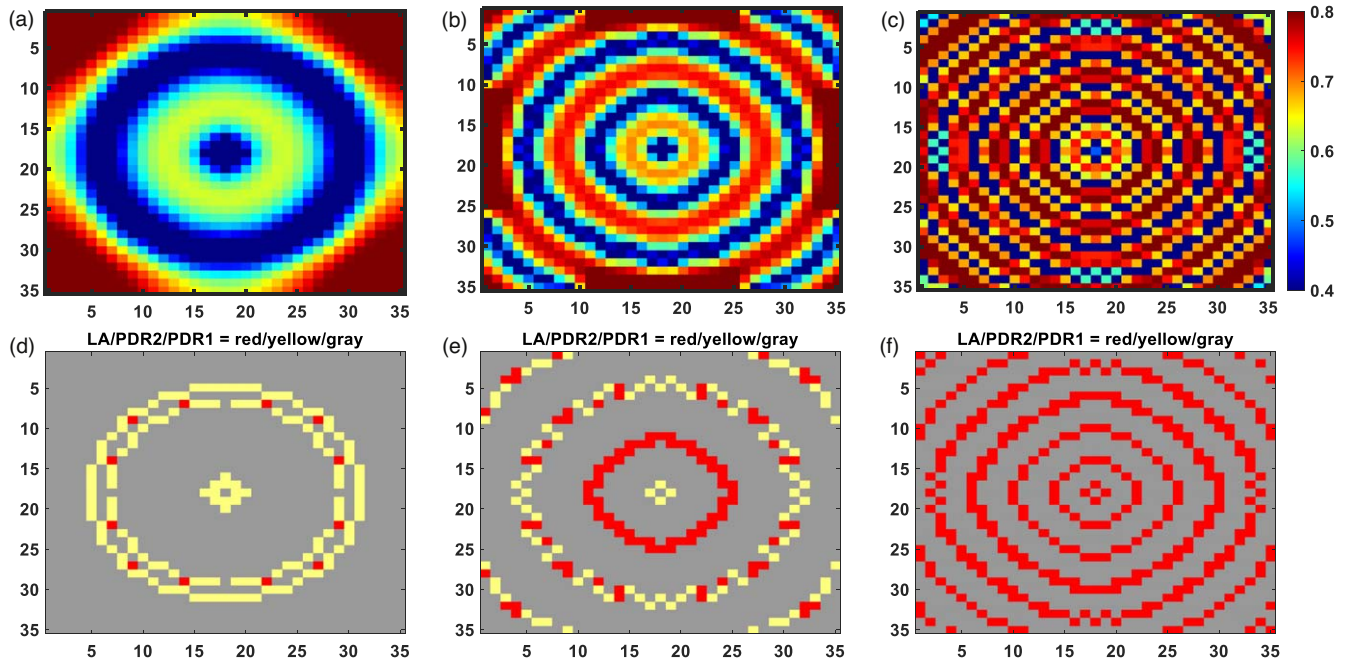


**Fig. 9.** (Color online) Simulation results of a  $35 \times 35$  MCNN structure for  $I_b = 100 \mu\text{A}$ ,  $R_b = 50 \text{k}\Omega$ ,  $C = 10 \text{fF}$  while we set  $R_c = 0.5 \text{k}\Omega$  in (a),  $R_c = 2.5 \text{k}\Omega$  in (b), and  $R_c = 10 \text{k}\Omega$  in (c). All the cells have the same initial condition, except for the one in the center of the network. As the coupling strength reduces, the color contrast between neighboring cells increases, indicating a sharper transition between their memristor voltage amplitudes at steady state. The effect of the coupling strength on the location of the cell equilibria is illustrated in the ternary maps, shown in plots (d)–(f), where a red, yellow, and gray pixel represents a cell equilibrium, lying along the LA, or PDR2, or PDR1 branch, respectively. Comparing plots (d), (e), and (f), it can be realized that, as the coupling resistance is increased, those cell equilibria, originally lying along the PDR2 branch, are progressively forced to move to the LA branch.

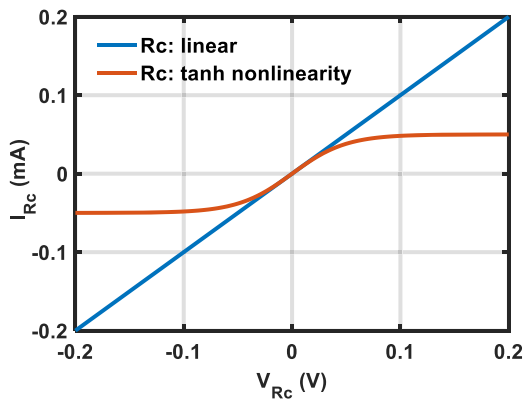


**Fig. 10.** (Color online) Red (blue) curve: current–voltage characteristic of a coupling resistor with tanh nonlinearity (with linear constitutive relationship).

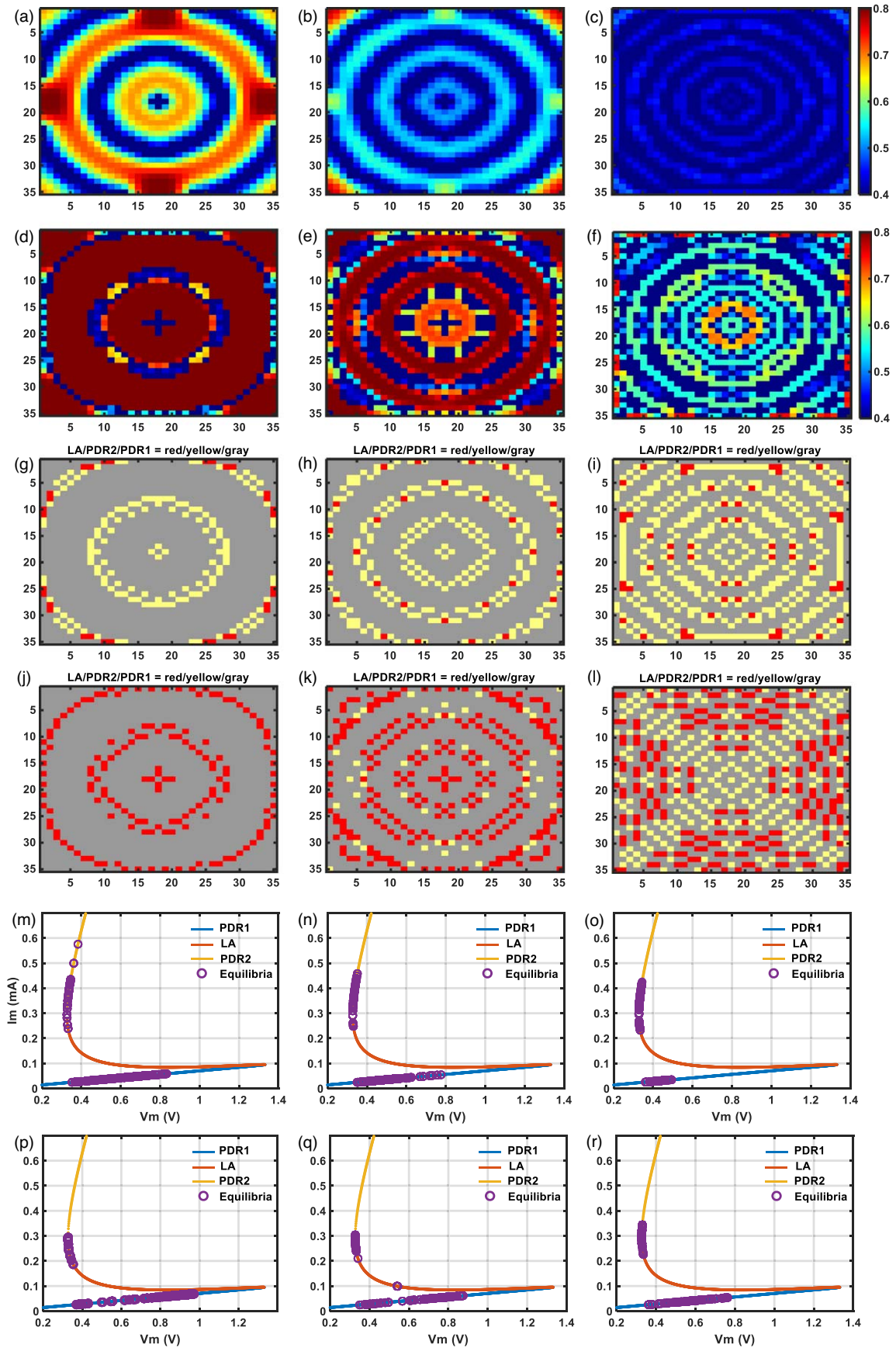
lie along the PDR1 region of the  $I_m$ – $V_m$  locus, as indicated by the gray pixels, some of them are located along the PDR2 region of the  $I_m$ – $V_m$  locus, as indicated by the yellow pixels, while only a few of them sit on the LA region of the  $I_m$ – $V_m$  locus, as indicated by the red pixels. On the other hand, increasing the coupling resistance progressively moves the cell equilibrium points, lying originally along the PDR2 region, into the LA region [see Fig. 9(e)], till a point, where cell equilibria may no longer be found on the upper locally-passive branch [see Fig. 9(f)].

Figure 11 demonstrates the strong impact that a tanh-based nonlinearity in the resistive coupling element has on the characteristics of the patterns emerging in the network. Comparing Figs. 11(a)–11(c) with Figs. 11(d)–11(f), it can be concluded that the nonlinear coupling creates new geometric features, e.g. vertical and horizontal paths, in the static patterns, enhancing their dynamic range, and the

strengthening the color contrast across them, which certainly facilitates their classification. The implications of introducing a nonlinearity in the couplings between the MCNN cells can be further explored through a comparison between Figs. 11(m)–11(o) and Figs. 11(p)–11(r). It is clearly appreciable that the cell equilibria, sitting along the PDR2 region of the DC  $I_m$ – $V_m$  characteristic in the linear coupling scenarios, move into the LA region of the same characteristic, accumulating over a comparatively-narrower voltage range, in the nonlinear coupling simulations. On the contrary, the cell equilibria, located on the PDR1 region of the DC  $I_m$ – $V_m$  characteristic in the linear coupling scenarios, spread across a relatively-larger voltage range, in the nonlinear coupling simulations, which explains the increment in the dynamic range of the patterns, appearing in the network in the latter cases.

It is worth observing that a tanh nonlinearity, featured by the coupling resistor in the simulations, can be physically realized by exploiting the saturation characteristics of MOSFET transistors operating in the ohmic regime. Finally, the bistability of the basic cell under suitable bias conditions, e.g. under each  $I_b$  value in the set  $\{100, 110\} \mu\text{A}$ , for  $R_b = 50 \text{k}\Omega$  (refer to Fig. 7), can be employed to assign well defined initial conditions other than the operating point, to cell groups across the MCNN.

Figure 12 reveals the link between the transients of the cell capacitor voltages and the resulting steady-state pattern characteristics. Focusing first on the smooth pattern, shown in Fig. 12(a), the cell capacitor voltages are found to exhibit a relatively-low degree of ripple in amplitude, and to settle down to the respective steady-state solutions rather quickly, in about 5 ns, while covering a limited range with a homogenous distribution, as illustrated in Fig. 12(b).



**Fig. 11.** (Color online) Simulation results of a  $35 \times 35$  MCNN structure for  $R_b = 50 \text{ k}\Omega$ ,  $C = 10 \text{ fF}$  where the local coupling is established through  $R_c = 1 \text{ k}\Omega$  in (a)–(c), (g)–(i) and (m)–(o), or the constitutive relationship  $I_{R_c} = 5 \cdot 10^{-5} \cdot \tanh(20 \cdot V_{R_c})$  in (d)–(f), (j)–(l) and (p)–(r). In addition,  $I_b = 100 \mu\text{A}$  for the patterns in the first column,  $I_b = 110 \mu\text{A}$  for the second column and  $I_b = 150 \mu\text{A}$  for the last column. It can be seen from (d)–(f) that the choice of tanh nonlinearity in the coupling resistor enhances the contrast and the dynamic range, and therefore the visibility, of the patterns, while creating new geometric features facilitating their classification. Comparing ternary patterns of (g)–(i) and (j)–(l), it can be observed that yellow pixels are rather replaced by red pixels, implying that nonlinear coupling forces the equilibria in PDR2 region to move to LA region. This effect can also be observed by comparing the distribution of equilibria on  $I_m$ – $V_m$  loci in (m)–(o) with (p)–(r) while the equilibria moving from PDR2 to LA accumulate in a relatively-narrower line segment on the  $I_m$ – $V_m$  curve, while the equilibria located PDR1 region are spread across a relatively-wider range, resulting in an increased dynamic range for the patterns.

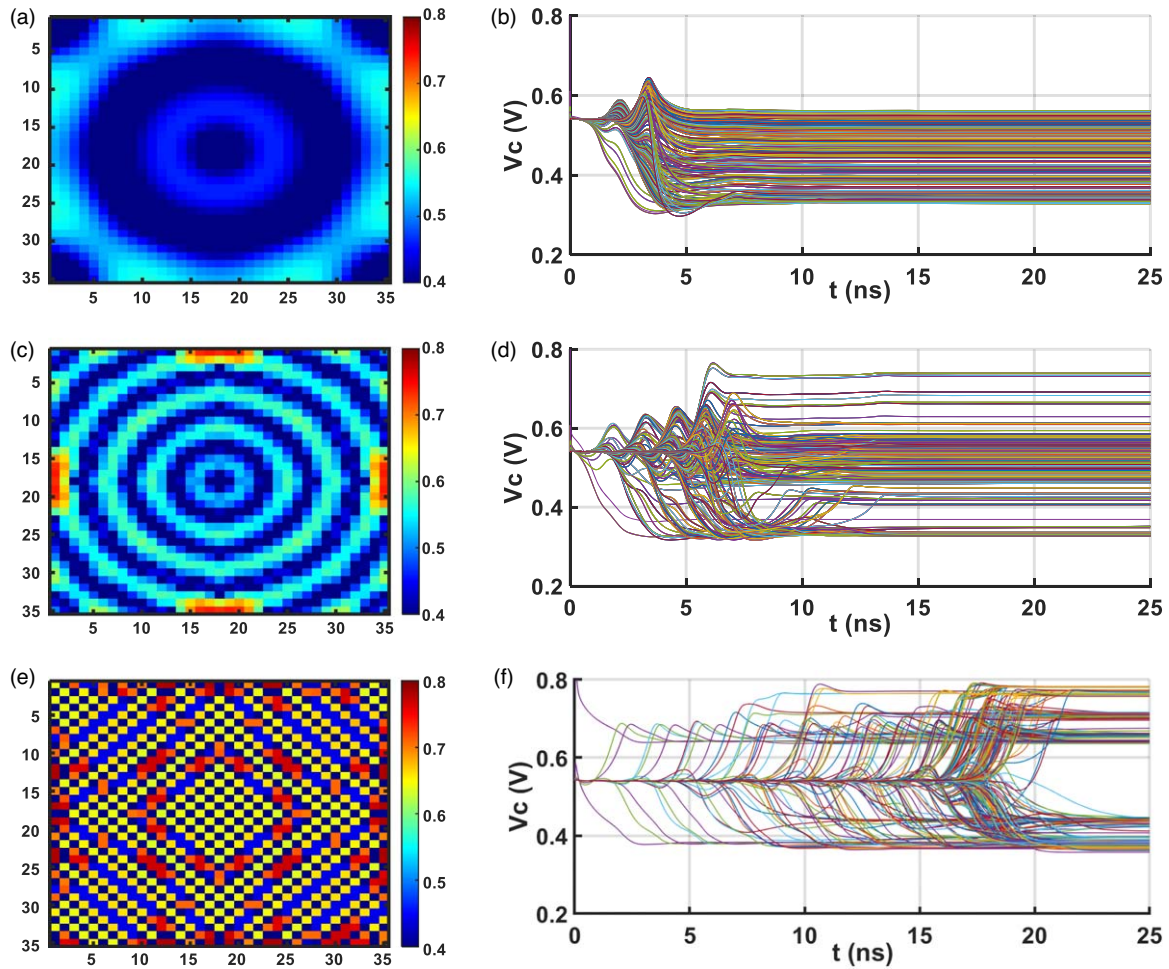


**Fig. 12.** (Color online) Simulation results of a  $35 \times 35$  MCNN structure where transient characteristics of cell capacitor voltages are depicted for three different patterns. For all patterns,  $I_b = 110 \mu\text{A}$ ,  $R_b = 50 \text{ k}\Omega$ ,  $C = 10 \text{ fF}$  whereas  $R_c = 0.2 \text{ k}\Omega$  in (a)–(b),  $R_c = 2 \text{ k}\Omega$  in (c)–(d), and  $R_c = 20 \text{ k}\Omega$  in (e)–(f). For the smooth pattern given in (a), the cell capacitor voltages exhibit relatively-lower degree of ripple in amplitude and settle down to the respective steady-state solutions rather quickly, while covering a limited voltage range with a homogenous distribution, as shown in (b). In regard to the pattern illustrated in (c), which can be characterized by relatively-sharper color transitions between neighboring cells, the capacitor voltages feature a higher degree of ripple in amplitude, and exhibit a longer settling time during the transient process, converging to steady states distributed non-uniformly over a rather wide range, as given in (d). For the pattern with sharpest color contrast, as depicted in (e), the capacitor voltages in (f) feature the highest degree of ripple in amplitude, while requiring the longest settling time to approach the steady state, while their asymptotic values clearly display the most uneven distribution.

Resulting from a reduction in the coupling strength, the pattern depicted in Fig. 12(c) clearly features sharper color transitions between neighboring cells as compared to the pattern in Fig. 12(a). This stems from the higher degree of ripple in amplitude, which the cell capacitor voltages from Fig. 12(d) feature relative to their counterparts in Fig. 12(b). In comparison to the time waveforms in Fig. 12(b), the capacitor voltages from Fig. 12(d) further exhibit a longer settling time, about 10 ns, and are found to cover a wider range with a less uniform distribution. Finally, the pattern with the sharpest color contrast—refer to Fig. 12(e)—emerges across the MCNN as the capacitor voltages, shown in Fig. 12(f), are subject to the largest amplitude ripple as they converge through the longest settling time, i.e. around 20 ns, to the respective steady states, which clearly cover the largest range, displaying the most uneven distribution.

#### 4. Conclusions

In this work, we investigated pattern formation dynamics across a MCNN employing locally active memristors. We

implemented a variable transformation in the Pickett model as a novel technique to improve its numerical stability and reduced the simulation time. Then, including parasitic resistances, we obtained a  $\text{VO}_2$  memristor model with multiple segments in the locally active region and showed how to exploit its AC equivalent circuit to conduct a simple and efficient analytical investigation of stability properties and locally active dynamics for the single device and for the single cell of the proposed MCNN. By varying the cell capacitance value, we witnessed the formation of different patterns, which reveals the impact of transient behavior of the capacitor voltages on the emergent phenomena. Later on, to get a better understanding of the pattern characteristics, we introduced a novel approach based upon the derivation of ternary pattern maps, where each pixel contains the information of the location of the static equilibria located on a specific region of the DC  $I_m$ – $V_m$  characteristic from a set of three possible branches. We conjecture that, in the future, these ternary pattern maps can also be employed for a fast detection and classification of emergent phenomena in

MCNNs. Furthermore, we considered a tanh nonlinearity for the constitutive relationship of the coupling resistor and showed how this improves the contrast in the patterns.

As a future work, it can be fruitful to investigate the impact of other kinds of nonlinearities for the constitutive relationships of the coupling resistor as well as of the bias resistor, which can introduce further control parameters to adjust the distribution of the DC equilibria of the cells' memristors along the DC  $I_m$ - $V_m$  characteristic of the VO<sub>2</sub> device. While, in this work, we have particularly focused on a VO<sub>2</sub> memristor model, the mathematical framework, conceived by Pickett, is sufficiently general to capture the dynamics of other devices including NbO Mott memristors<sup>42)</sup> or ovonic threshold switches (OTS).<sup>43)</sup> Therefore, the analysis and design procedure introduced in parametric form in this paper, for the investigation of pattern formation dynamics in MCNNs, can be adopted to describe similar phenomena in arrays based upon other locally active resistance switching memories.<sup>44)</sup> In general, we conjecture that comparable results, allowing to draw qualitatively similar conclusions, may be obtained for array designs centered around any NDR device from a broad class.

### Acknowledgments

This work was supported by the German Research Foundation (DFG) under the Project No. 411647366 and Project No. 379950170.

### Appendix

The parameter values of the model equations given by Eqs. (8)–(11) and employed during the numerical simulations can be found in Table A-I.

**Table A-I.** Parameter values of the model equations given by Eqs. (8)–(11).

$g_0$	$g_1$	$g_c$	$x_a$	$x_s$
$9.852 \cdot 10^{-6}$	$3.28 \cdot 10^{-2}$	$9.4562 \cdot 10^{-7}$	100	300
$C_c$	$k$	$R_p$	$R_s$	
$7 \cdot 10^{-16}$	6.6244	$16 \cdot 10^3$	400	

### ORCID iDs

Ahmet Samil Demirkol  <https://orcid.org/0000-0002-1236-1300>

- 1) J. Shalf, *Phil. Trans. R. A* **378**, 20190061 (2020).
- 2) T. N. Theis and H.-S. P. Wong, *Comput. Sci. Eng.* **19**, 41 (2017).
- 3) D. Strukov, G. Snider, D. Stewart, and S. Williams, *Nature* **453**, 80 (2008).
- 4) L. Chua, *IEEE Trans. Circuit Theory* **18**, 507 (1971).
- 5) A. Sebastian, M. Le Gallo, R. Khaddam-Aljameh, and E. Eleftheriou, *Nat. Nanotechnol.* **15**, 529 (2020).
- 6) D. Ielmini and G. Pedretti, *Adv. Intell. Syst.* **2**, 2000040 (2020).
- 7) Y. Li and K.-W. Ang, *Adv. Intell. Syst.* **3**, 2000137 (2021).
- 8) H. Kim, M. R. Mahmoodi, H. Nili, and D. B. Strukov, *Nat. Commun.* **12**, 5198 (2021).

- 9) K. A. Ali, M. Rizk, A. Baghdadi, J.-P. Diguët, J. Jomaah, N. Onizawa, and T. Hanyu, *IEEE Trans. Very Large Scale Int. (VLSI) Syst.* **28**, 2370 (2020).
- 10) B. Zhang et al., *Nat. Commun.* **12**, 1984 (2021).
- 11) M. Pickett, G. Medeiros-Ribeiro, and R. Stanley Williams, *Nat. Mater.* **12**, 114 (2013).
- 12) J. del Valle, P. Salev, Y. Kalcheim, and I. K. Schuller, *Sci. Rep.* **10**, 4292 (2020).
- 13) I. Boybat, M. Le Gallo, S. R. Nandakumar, T. Moraitis, T. Parnell, T. Tuma, B. Rajendran, Y. Leblebici, A. Sebastian, and E. Eleftheriou, *Nat. Commun.* **9**, 2514 (2018).
- 14) L. F. Abbott and P. Dayan, *Theoretical Neuroscience: Computational and Mathematical Modeling of Neural Systems* (MIT Press, Cambridge, MA; London, 2001).
- 15) W. Gerstner, W. M. Kistler, R. Naud, and L. Paninski, *Neuronal Dynamics: From Single Neurons to Networks and Models of Cognition* (Cambridge University Press, Cambridge, 2014).
- 16) L. F. Abbott, *Brain Res. Bull.* **50**, 303 (1999).
- 17) C. Mead, *Analog VLSI and Neural Systems* (Addison-Wesley, Reading, MA, 1989).
- 18) G. Indiveri et al., *Front. Neurosci.* **5**, 73 (2011).
- 19) L. Chua and L. Yang, *IEEE Trans. Circuits Syst.* **35**, 1273 (1988).
- 20) L. Chua, *CNN: A Paradigm for Complexity* (World Scientific Publishing Co., Singapore, 1998), Vol. 31.
- 21) T. Roska, L. Chua, D. Wolf, and T. Kozek, *IEEE Trans. Circuits Syst. I* **42**, 807 (1995).
- 22) P. Arena, L. Fortuna, and M. Branciforte, *IEEE TCAS I: Fund. Th. App.* **46**, 253 (1999).
- 23) L. Chua, *Int. J. Bifurcation Chaos* **15**, 3435 (2005).
- 24) D. Walgraef, *Spatio-Temporal Pattern Formation with Examples from Physics, Chemistry, and Materials Science* (Springer, New York, NY, 1997).
- 25) A. M. Turing, *Proc. Trans. R. Soc.* **237**, 37 (1952).
- 26) J. D. Murray, *Mathematical Biology: I. An Introduction* (Springer, New York, 2003).
- 27) A. Buscarino, C. Corradino, L. Fortuna, and M. Frasca, *Chaos* **29**, 103145 (2019).
- 28) M. Weiher, M. Herzig, R. Tetzlaff, A. Ascoli, T. Mikolajick, and S. Slesazek, *IEEE Trans. Circuits Syst. I* **66**, 2627 (2019).
- 29) A. S. Demirkol, A. Ascoli, I. Messaris, and R. Tetzlaff, *IEEE Int. Symp. on Circuits and Systems (ISCAS)*, 2021, 10.1109/ISCAS51556.2021.9401280.
- 30) A. Ascoli, S. Slesazek, H. Mähne, R. Tetzlaff, and T. Mikolajick, *IEEE Trans. Circuits Syst. I* **62**, 1165 (2015).
- 31) A. S. Demirkol, A. Ascoli, and R. Tetzlaff, 2021 17th Int. Workshop Cellular Nanoscale Networks and their Applications (CNNA), 2021, 10.1109/CNNA49188.2021.9610811.
- 32) W. Yi, K. K. Tsang, S. K. Lam, X. Bai, J. A. Crowell, and E. A. Flores, *Nat. Commun.* **9**, 4661 (2018).
- 33) M. D. Pickett and R. S. Williams, *Nanotechnology* **23**, 215202 (2012).
- 34) G. A. Gibson et al., *Appl. Phys. Lett.* **108**, 023505 (2016).
- 35) S. Slesazek, H. Mahne, H. Wylezich, A. Wachowiak, J. Radhakrishnan, A. Ascoli, R. Tetzlaff, and T. Mikolajick, *RSC Adv.* **5**, 102318 (2015).
- 36) A. Ascoli, A. S. Demirkol, R. Tetzlaff, S. Slesazek, T. Mikolajick, and L. Chua, *Front. Neurosci.* **15**, 651452 (2021).
- 37) Y. Liang, Q. Zhu, G. Wang, S. K. Nath, H. H.-C. Iu, S. K. Nandi, and R. G. Elliman, *IEEE Trans. Circuits Syst. I* **69**, 1278 (2022).
- 38) I. Messaris, T. D. Brown, A. S. Demirkol, A. Ascoli, M. M. Al Chawa, R. S. Williams, R. Tetzlaff, and L. Chua, *IEEE Trans. Circuits Syst. I* **68**, 4979 (2021).
- 39) F. F. Kuo, *Network Analysis and Synthesis* (Wiley, Singapore, 1966).
- 40) A. S. Demirkol, A. Ascoli, I. Messaris, and R. Tetzlaff, *Memristor—An Emerging Device for Post-Moore's Computing and Applications* (IntechOpen, London, United Kingdom, 2021).
- 41) A. Ascoli, A. S. Demirkol, R. Tetzlaff, and L. Chua, *IEEE Trans. Circuits Syst. I* **69**, 1252 (2022).
- 42) S. Kumar, J. Strachan, and R. Williams, *Nature* **548**, 318 (2017).
- 43) S. Zhang, H. Xu, Z. Li, S. Liu, B. Song, and Q. Li, *Front. Neurosci.* **15** (2021).
- 44) A. Ascoli, A. S. Demirkol, R. Tetzlaff, and L. Chua, *IEEE Trans. Circuits Syst. I*, 2022, 10.1109/TCSI.2022.3194465.